THE JOURNAL OF PHYSICAL CHEMISTRY C
A JOURNAL OF THE AMERICAN CHEMICAL SOCIETY

pubs.acs.org/JPCC

Article

Morphological Evolution of Monolayer MoS_2 Single-Crystalline Flakes

Qingxuan Li, Lei Zhang, Chengyao Li, Jie He, Yifan Wei, Jinzhu Zhao, Ruili Zhang, Peng Wang, Shaojie Fu, Fei Chen, Ruwen Peng,* and Mu Wang*

Cite This: *J. Phys. Chem. C* 2022, 126, 3549−3559

Read Online

ACCESS | Metrics & More | Article Recommendations | Supporting Information

ABSTRACT: Understanding and controlling the growth morphology of two-dimensional crystals of transition metal dichalcogenides (TMDs) is essential in developing high-quality crystalline material for spintronics, valleytronics, electronics, and optics. Here we report our studies on the evolution of crystallite morphology of MoS_2 observed in chemical vapor deposition. It is shown that as time goes on, the growth morphology of MoS_2 flakes undergoes a transition from a triangle to a star shape, then back to a triangle, and finally to a bulgy irregular morphology. By tuning the temperature of the element sources, the atomic ratio of S and Mo on the growing interface can be adjusted. The variation of the S/Mo ratio affects the edge diffusion length and nucleation behavior on the edge of crystallite, leading to different growth morphologies. Our observations provide clues on how to engineer the morphology and control the quality of TMD crystalline sheets.

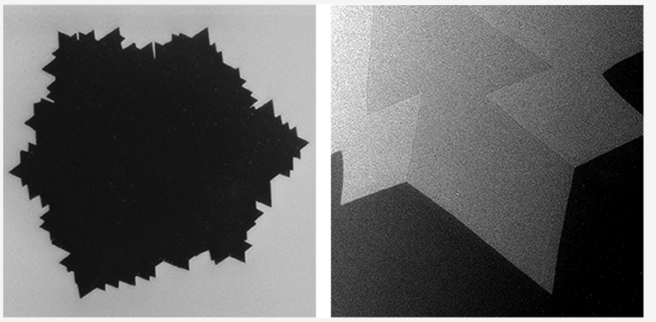

INTRODUCTION

Transition metal dichalcogenides (TMDs) have shown great application potential in optoelectronics, valleytronics, and catalysis owing to their direct bandgap in monolayer, strong spin-valley coupling, and highly active catalytic sites at edges.[1−5] To date, chemical vapor deposition (CVD) is the most often applied approach to achieve large-area monolayer or multilayer TMD films.[6−9] One of the distinct features is that the morphology of TMD crystallites is very rich in the CVD fabrication, which varies from triangles to hexagons, dendrites, irregular star-like, and nanoribbons, etc., depending on the specific growth conditions.[10−17] On the other hand, many material properties and functional performance of the TMD materials are highly dependent on the geometrical shape and microstructures.[18−23] For example, the edge magnetism of the monolayer MoS_2 flakes arises in the dodecagonal and hexagonal shape but disappears in the triangular shape.[19] Unlike compact MoS_2 triangles, MoS_2 dendrites possess abundant active edge sites with rather high catalytic capabilities in hydrogen evolution reactions.[20] Moreover, crystallographic defects in two-dimensional (2D) materials may lead to interesting physical properties, such as edge nonlinear optics,[24] unique bandgap tunability,[25] and oscillating edge states.[26] Theoretical studies indicate that the zigzag edges of TMDs exhibit metallic and ferromagnetic characteristics.[21,27,28] So far, an in-depth understanding of the evolution mechanism and controlling approach of 2D crystal morphology remains challenging, yet it is a fundamental issue of low-dimensional material studies.

It is helpful to understand the growth mechanisms of TMDs to achieve the desired morphology with the desired size. Many efforts have been devoted to exploring the growth mechanisms of TMD crystals in recent decades.[29−35] In the thermodynamic equilibrium regime, classical Wulff construction has been applied to reveal the shape evolution mechanism of MoS_2 crystals from triangles at the sulfur-rich condition to hexagons at the molybdenum-rich condition.[19,29] It has been reported that the formation mechanism of dendritic patterns of 2D materials could be described by the diffusion-limited aggregation model.[30,34] On the other hand, TMD materials also develop in the kinetic regime. Recently, the vapor−liquid-adatom-solid model has been introduced to explain the growth mechanism of MoS_2 flakes with high-index edges.[36] Besides, various nonequilibrium shapes of TMD crystals have been studied recently.[14,32,33] Despite all these efforts, however, a guideline to control the morphology evolution of TMD crystals remains elusive.

Received: December 6, 2021
Revised: January 27, 2022
Published: February 10, 2022

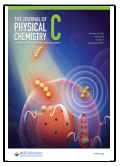

This article reports on the growth of monolayer MoS_2 with a modified CVD method on optical glass using ammonium heptamolybdate and sulfur powder as precursors. When the temperature of sulfur powder is set to 140 °C and the substrate temperature is set to 800 °C, the shape of MoS_2 flakes evolutes from triangular to three-point stars, then to triangular, and finally to a bulgy irregular shape as the growth time extends. To the best of our knowledge, this is the first report on the evolution of MoS_2 flakes from faceted triangles to rough, bulge ones. Structural analysis indicates that the MoS_2 flakes with three-point-star shape and triangular shape are all single-crystalline; the bulgy irregular-shaped MoS_2 flakes contain a large number of grain boundaries and are essentially polycrystalline. Besides, by increasing the temperature of sulfur powder, we observe that the nucleation at the edge of the crystallite becomes easier, and MoS_2 crystallite transforms from a triangular shape to a bulgy irregular shape much faster. The first-principles calculations indicate MoS_2 clusters are easier to nucleate at the center of the flake edges than in the corner region of the triangular flake. Photoluminescence measurements show that the luminescence intensity of MoS_2 flakes strongly relates to the flake morphology. We suggest that our study provides a clue to control the morphology of TMDs for technological applications.

METHODS

The MoS_2 crystalline flakes are grown in a homemade multi-temperature-zone tubular furnace. Ammonium heptamolybdate ($(NH_4)_6Mo_7O_{24} \cdot xH_2O$, AHM) (Aladdin, purity 99.5%) and sulfur powder (Aladdin, purity 99.95%) are used as precursors. Before growth, the optical glass (HK-9 L, 1.5 × 1.5 cm^2) is cleaned in H_2SO_4/H_2O_2 and is rinsed thoroughly with deionized(DI) ultrapure water (Millipore, electric resistivity 18.2 MΩ·cm). Sulfur powder (500 mg) is loaded in an alumina boat and placed upstream. The AHM solution (0.025 mg/mL) is dropped on the cleaned glass substrates and placed downstream about 45 cm away from the alumina boat. The typical temperature of sulfur powder is raised to 140 °C in 25 min. At the same time, the glass substrate is heated to 800 °C from room temperature within 25 min. The whole growth process is carried out at ambient pressure with 50 sccm of flowing ultrapure N_2 as the carrier gas, and the growth time varies from several minutes to 20 min. By comparing the difference between the amount of sulfur powder before and after the crystal growth, we find that less than 1% of the initial load of sulfur powder has been evaporated when the source temperature of the sulfur powder is set as 140 °C.

The as-grown MoS_2 flakes can be transferred onto substrates using the following transfer method. First, a poly(methylmethacrylate) (PMMA) layer is spin-coated on the MoS_2/glass at 2000 rpm for 1 min. Then the edges of the PMMA layer are scraped off with a blade, and the PMMA/MoS_2/glass is then immersed in DI water to peel off the PMMA/MoS_2 film from the glass substrate. After that, the PMMA/MoS_2 film is transferred onto the target substrate. Finally, the PMMA is removed by acetone. For TEM and STEM characterizations, the PMMA/MoS_2 film is collected by the grid while the other operation processes remain precisely the same.

To understand the nucleation mechanism on the edge of MoS_2 crystallite, we perform the first-principles calculations using the Vienna ab initio simulation package (VASP) based on density functional theory (DFT). The core−valence interactions are treated by the projector augmented wave (PAW) method, where the plane wave expansion is truncated with a cutoff energy of 300 eV. We apply the generalized gradient approximation (GGA) with the Perdew−Burke−Ernzerhof (PBE) scheme as the exchange-correlation function. The convergence tolerance for the self-consistent-field iteration was set as 10^{-5} eV. A vacuum layer larger than 14 Å was used to avoid the spurious interaction between two adjacent clusters. In momentum space, a two-dimensional 1 × 1 k-grid is used in self-consistent calculations for all studied supercells. All the structures are relaxed until the forces on each atom are below 0.02 eV/Å.

The morphology of the monolayer MoS_2 flakes is characterized using an optical microscope (Nikon, ECLIPSE 80i), a multimode atomic force microscope (Digital Instruments, Nanoscope IIIa), and a field-emission scanning electron microscope (Zeiss, ULTRA 55), respectively. The structure of the MoS_2 flakes is investigated by transmission electron microscopy (Tecnai F20) and double spherical aberration-corrected scanning transmission electron microscopy (Titan 60−300). Raman and photoluminescence spectra are obtained by a confocal micro-Raman system (Princeton Instruments) with the laser excitation wavelength as 532 nm.

RESULTS

The optical micrograph of the MoS_2 flakes grown on the glass substrate is illustrated in Figure 1a. The triangular flakes are

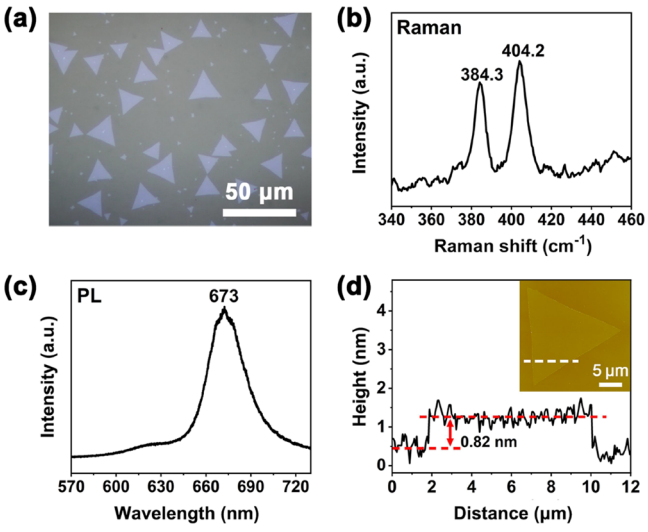

Figure 1. (a) Optical image of MoS_2 flakes grown on optical glass. (b) Raman spectrum, (c) Photoluminescence spectrum of MoS_2 monolayer. (d) AFM micrographs and height profiles of a MoS_2 flake transferred onto SiO_2/Si substrate. The height profile is obtained along the dashed line in the inset.

the as-grown MoS_2 crystallites, which possess uniform contrast and are evenly dispersed on the substrate. The darker background is the glass substrate. We use Raman and photoluminescence (PL) spectra to determine the thickness and optical properties of the MoS_2 flakes. As shown in Figure 1b, the Raman spectra have two peaks at 384.3 cm^{-1} (E^1_{2g} mode) and 404.2 cm^{-1} (A_{1g} mode), respectively, which are the hallmark features of MoS_2 crystals. The frequency difference between E^1_{2g} mode and A_{1g} mode is determined by the number of layers of MoS_2, and the value of the frequency difference for MoS_2 monolayer is about 20 cm^{-1} in previous

https://doi.org/10.1021/acs.jpcc.1c10342
J. Phys. Chem. C 2022, 126, 3549−3559

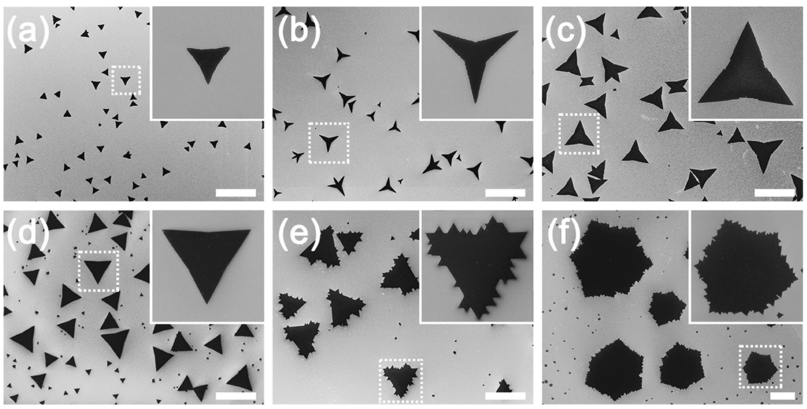

Figure 2. SEM micrographs of different morphologies of MoS_2 flakes transferred onto Si substrates. MoS_2 flakes were grown with the temperature of S source set as 140 °C, and the growth time was (a) 4 min, (b) 6 min, (c) 8 min, (d) 10 min, (e) 12 min, and (f) 15 min, respectively. The insets are the enlarged micrographs of the flake marked by the white dashed frame. The scale bar represents 30 μm.

studies.[9,10,37] In our experiments, the frequency difference between these two modes is 19.9 cm^{-1}, suggesting that the flake is indeed a monolayer. The typical PL spectra of MoS_2 flakes (Figure 1c) show a sharp peak at 673 nm, which matches well with the direct excitonic transition of the MoS_2 monolayer.[10,18,38] Figure 1d demonstrates the atomic force micrograph (AFM) and height profile of a MoS_2 flake after being transferred on a SiO_2/Si substrate. The height profile reveals the thickness of the flake is 0.82 nm, which is in agreement with the known values of the MoS_2 monolayer (0.77 nm).[9]

In our experiments, we observe that the morphology of MoS_2 flakes changes with growth time. To monitor the morphological evolution of the MoS_2 monolayer flakes, we take the growing sample out of the furnace at different growth times, and the as-grown MoS_2 flakes are transferred onto a Si substrate for SEM observation. Figure 2 shows the morphology of the as-grown MoS_2 flakes at different times when the temperature of the sulfur powder is set as 140 °C. The triangular MoS_2 flakes are initially nucleated on the glass substrate (Figure 2a). Then, the corner regions of the triangular MoS_2 flake develop faster than the central parts of the edges, leading to the three-point-star shape (Figure 2b). After that, as time goes on, the morphology of the MoS_2 flakes gradually evolves from three-point stars back to triangles (Figure 2c,d). As the growth continues, the newborn nucleus appears randomly on the edges of the MoS_2 flakes, and the nucleation rate is higher in the central part of each edge (Figure 2e). In this way, the growth pattern gradually changes from a triangle to an irregular bulgy shape (Figure 2f).

To investigate the microstructure of MoS_2 flakes with different morphologies, we apply the selected-area electron diffraction (SAED), dark-field transmission electron microscopy (dark-field TEM), and scanning transmission electron microscopy (STEM). Figure 3a-c illustrates the bright-field TEM micrograph and SAED pattern of star-shaped, triangular-shaped, and bulgy irregular-shaped MoS_2 flakes. Figure 3d-f shows the corresponding dark-field TEM micrographs collected using a field diaphragm at the green, blue, and orange circles on the corresponding SAED pattern (Figure 3a-c, inset), respectively. As illustrated in the insets of Figure 3a,b, the SAED patterns all have sixfold symmetry. Furthermore, Figure 3d,e shows homogeneous contrast across the whole MoS_2 flakes, indicating that there are no grain boundaries across the crystallite, and the star-shaped and triangular-shaped

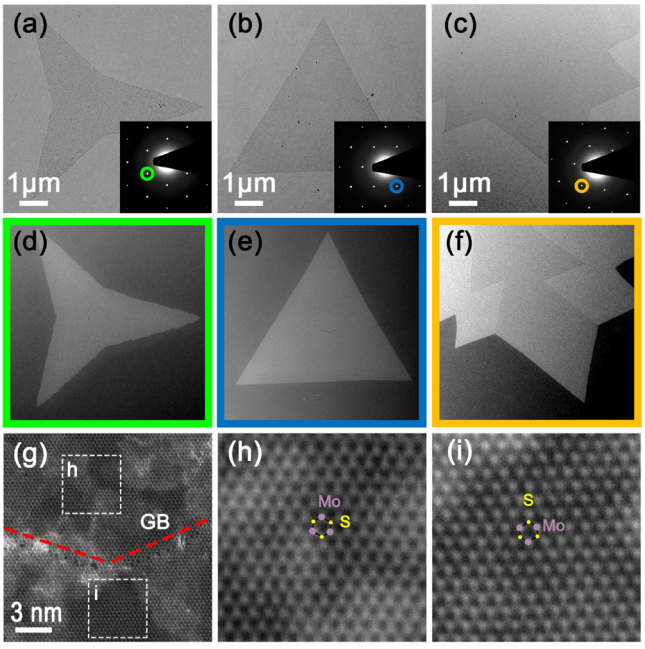

Figure 3. Bright-field TEM image of a MoS_2 (a) three-point star, (b) triangular, and (c) bulgy irregular shapes. The inset in (a–c) is the corresponding SAED pattern, which shows the sixfold symmetry. (d–f) Dark-field TEM images corresponding with the (d) green, (e) blue, and (f) orange circle in the corresponding SAED pattern, respectively. (g) STEM image of a grain boundary of bulgy irregular-shaped MoS_2 flakes. The red dashed lines highlight the grain boundary. (h) and (i) Enlarged images of the dashed white region in (g).

MoS_2 flakes are perfect single-crystalline. It is noteworthy that the SAED pattern of a bulgy irregular-shaped MoS_2 flake also shows one set of sixfold symmetric diffraction spots (Figure 3c). However, the corresponding dark-field TEM micrograph illustrates different contrast distributions (Figure 3f). This means that the bulgy irregular-shaped MoS_2 flake is comprised of multiple sets of twin crystalline regions. The regions with different contrast possess a parallelogram shape with the angle between adjacent edges as either 60 or 120°. Besides, the atomic structure of the bulgy irregular-shaped MoS_2 flakes is also characterized by STEM–high-angle annular dark-field (STEM-HAADF) images. Figure 3g shows a grain boundary in an irregular-shaped MoS_2 flake. The high-resolution STEM-HAADF images of the regions highlighted by the white frame

https://doi.org/10.1021/acs.jpcc.1c10342
J. Phys. Chem. C 2022, 126, 3549–3559

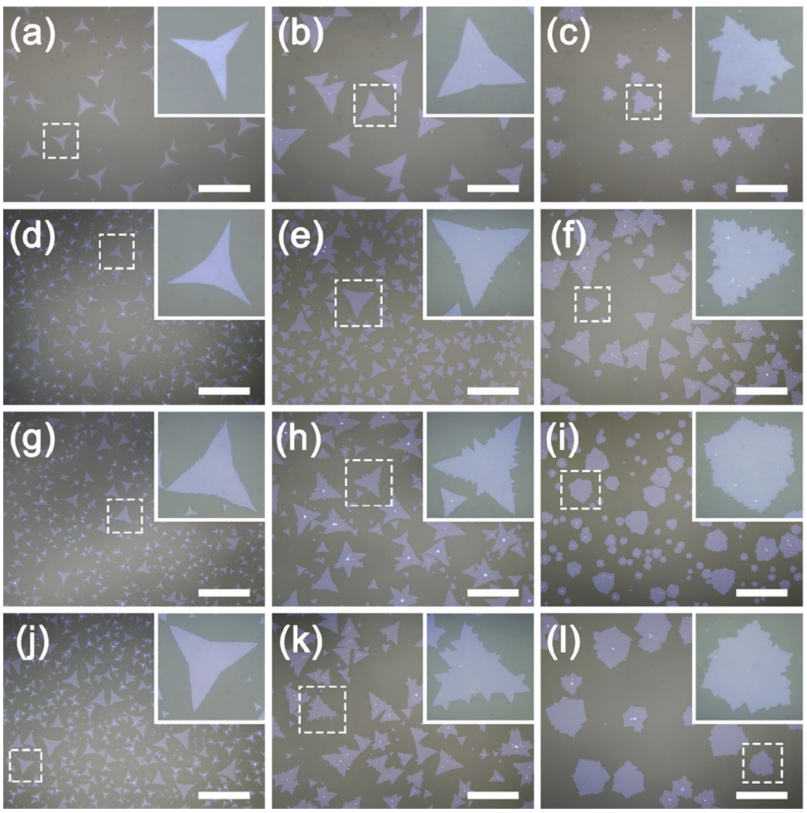

Figure 4. Optical images for morphological evolution of MoS_2 at a different time with different temperatures of sulfur powder. MoS_2 flakes were grown with the S temperature of 140 °C at growth times of (a) 6 min, (b) 8 min, (c) 12 min; with the S temperature of 160 °C at growth times of (d) 4 min, (e) 6 min, (f) 10 min; with the S temperature of 180 °C at growth times of (g) 4 min, (h) 6 min, (i) 10 min; with the S temperature of 200 °C at growth times of (j) 4 min, (k) 6 min, (l) 10 min. The insets are the magnified images of the white dashed frame. The scale bar represents 40 μm in (a–c) and 200 μm in (d–l).

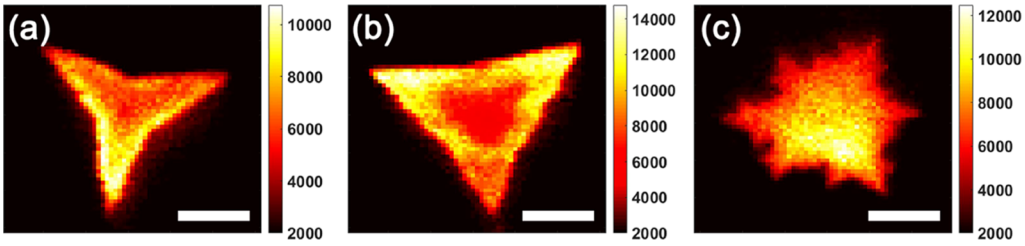

Figure 5. PL intensity mapping of MoS_2 of (a) three-point star, (b) triangular, and (c) irregular shapes. The scale bar represents 5 μm.

in Figure 3g show the hexagonal lattice of the MoS_2 monolayer (Figure 3h,i). The brighter spots correspond to Mo atoms, and the dimmer spots are the two stacked S atoms. Further analysis indicates that the lattice orientation of MoS_2 in Figure 3h has rotated 60° to that shown in Figure 3i, indicating the twinning relation of the two regions. This result is consistent with the dark-field TEM micrograph of the bulgy irregular-shaped MoS_2 flakes (Figure 3f). We therefore conclude that the bulgy irregular-shaped MoS_2 flakes are made of twin crystallites and are essentially polycrystalline.

We further carried out a series of experiments to explore the influence of the temperature of sulfur source on the morphological evolution of MoS_2 flakes. In our experimental system, the as-grown MoS_2 flakes are homogeneously dispersed on the substrate at each growth condition. The morphology of MoS_2 flakes grown at different sites across the centimeter-sized substrate is essentially the same (Figure S1 in the Supporting Information). Figure 4 illustrates the morphology of MoS_2 flakes at a specific time after the growth has been started at a certain temperature of the sulfur source. When the temperature of sulfur powder is at 140 °C (Figure 4a-c), the morphology of MoS_2 flakes changes from star shape to irregular shape in about 12 min. Our observation shows that no newborn nucleus appears on the edges of MoS_2 flakes when the growth continues for 8 min. When the temperature of sulfur powder is increased to 160 °C, very few newborn nuclei appear on the edges of the MoS_2 flakes in about 6 min (Figure 4e), and the morphology of MoS_2 flakes changes from star shape to irregular shape in 10 min (Figure 4f). When the temperature of sulfur powder is further increased to 180 °C, many triangular crystallites develop on the edges of the star-shaped MoS_2 flakes in 6 min (Figure 4h). Thereafter, MoS_2 flakes transform to the bulgy irregular shape when the growth has been started for about 10 min (Figure 4i). When the temperature of sulfur powder reaches 200 °C (Figure 4j-l), more significant numbers of triangular crystallites are formed

https://doi.org/10.1021/acs.jpcc.1c10342
J. Phys. Chem. C 2022, 126, 3549–3559

on the edges of the MoS_2 flakes in about 6 min, and MoS_2 flakes have been transformed to the bulgy irregular shape in about 10 min. Comparing with the morphological evolution processes of the MoS_2 flakes, we find that the nucleation on the edges of MoS_2 flakes becomes much easier at the higher temperature of the sulfur source. When the growth proceeds for 10 min, the higher sulfur temperature makes flake morphology deviate from the triangular pattern much more evidently.

It has been well established that crystalline defects may affect the optical properties of the crystallite. To verify this, we carry out photoluminescence spectroscopy measurements on the MoS_2 flakes with different shapes. The MoS_2 flakes with different morphologies possess a similar spectral profile in terms of peak position, indicating that the optical bandgap of star-shaped, triangular-shaped, and bulgy irregular-shaped MoS_2 flakes are essentially the same (Figure S2 in the Supporting Information). Figure 5 shows the PL intensity distribution of various shapes of MoS_2 flakes. For the MoS_2 flakes with a star shape and triangular shape, strong enhancement of PL intensity occurs at corners and edges (Figure 5a,b). However, strong PL intensity appears in the central part for the MoS_2 flakes with a bulgy irregular shape (Figure 5c). We further carry out photoluminescence mapping on the same MoS_2 flakes with different scanning directions. The results show that the inhomogeneous distribution of the photoluminescence across the MoS_2 flake is the intrinsic feature (Figure S3 in the Supporting Information).

DISCUSSION

MoS_2 monolayer possesses a hexagonal lattice structure, and hence triangular or hexagonal grains will be formed on the substrate depending on the interfacial energy. It has been reported that MoS_2 grown on graphene surface usually possesses a hexagonal shape,[39,40] whereas MoS_2 flakes grown on the surface of SiO_2 typically have a triangular shape.[18,41,42] Once a 2D grain is nucleated, the anisotropic edge free energy determines the final morphology of the MoS_2 flakes. The MoS_2 flakes are bounded by the two types of zigzag edges: Mo-terminated edges and S-terminated edges.[18,43,44] The edge free energy of Mo-terminated edges is lower than that of S-terminated edges in the sulfur-rich conditions.[43,44] On the SiO_2 surface, the growth rate of the S-terminated edge is faster than that of the Mo-terminated edge. Hence the S-terminated edges disappear gradually. Consequently, MoS_2 grains retain a regular triangle shape with Mo-terminated edges in a sulfur-rich atmosphere (Figure 6a).

In the growth of a triangular pattern, the corner regions usually develop faster and lead to the transition to the star shape (Figure 6b). It has been well established in crystallization that for a polyhedral crystal, the growth rate normal to a surface (edge) can be expressed as[45]

$$V = \beta(p)\sigma_s \quad (1)$$

where σ_s is the local supersaturation on the surface (or at the edge for 2D crystalline flake), β is the kinetic coefficient, and p is the local geometrical slope of the face (edge). Due to the geometrical shape of the crystallite, the gradient of the concentration field at the corner site of the polyhedral is higher than that at the center part of the facet (edge).[45−48] In the ideal situation, supersaturation at the corners of the polyhedral crystal, $\sigma_s(1)$, is the largest and the supersaturation at the center of the surface, $\sigma_s(0)$, is the smallest. Such an inhomogeneous distribution of supersaturation, $\delta\sigma = \sigma_s(1) - \sigma_s(0)$, is responsible for the faster growth rate at the corner of the polyhedral crystal,[46,48] and eventually leads to the deformation of the polyhedral.

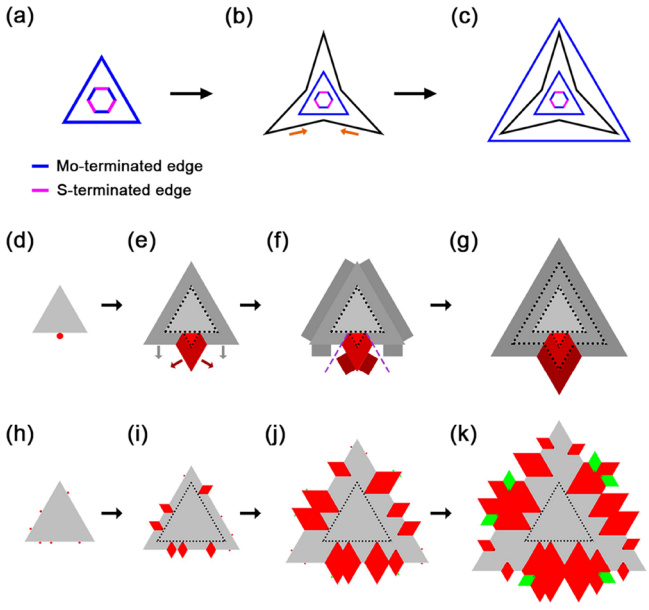

Figure 6. (a−c) Schematic plots of the morphology of MoS_2 flake changing from a triangle to a star shape and then back to a triangle. The orange arrows in plot b denote the movement direction of the steps initiated on the tips. (d−g) The model of twin boundaries propagation and morphological evolution process for the triangular MoS_2 flake with epitaxial nucleation at the edge. The solid red circle represents the newborn nucleus. The crimson and gray arrows in plot e represent the edge growth direction of the newborn crystallite and that of the original MoS_2 flake, respectively. The purple dashed lines in plot f mark the position of twin boundaries when two crystallites merge. The black dotted lines outline the crystalline shape at different moments. (h−k) Schematic illustration of the formation of the bulgy irregular-shaped MoS_2 flake originating from the triangle. The red and green regions represent the crystallites formed as different generations. The black dotted lines outline the border of the triangular MoS_2 flake at the initial moment.

On the other hand, however, the kinetic coefficient β is proportional to the local slope.[46] The slope of a face is a quantity of inclination to the vicinal face. It is known that the steeper a face is, the higher the step density will be on the face. This means that the sharpening of the tips of a triangular flake increases the local step density around the tip, which in turn makes the local mass consumption rate (growth rate) even higher if the nutrient supply is sufficient. It follows that in the far-from-equilibrium scenario with adequate nutrient supply, the corner will grow faster and faster and eventually develop into a fractal pattern.[49,50] In the diffusion-limited scenario, however, the nutrient transfer is constrained. The sharpening of the tips of the triangular flake increases the local step density in the tip regions. The consumption of nutrients by growing tips will decrease local supersaturation. This process decelerates the further sharpening of the corners. As the development of the steps toward the edge center, the step density on edge will gradually decrease. Eventually, the star-shaped flake will change back to a triangular shape (Figure 6c). There also exists the possibility that the slope of the star-shaped flakes resumes at a specific value, where the nutrient consumption caused by the growth of step is balanced by the

https://doi.org/10.1021/acs.jpcc.1c10342
J. Phys. Chem. C 2022, 126, 3549−3559

nutrient supply provided by the diffusion-limited system. In this scenario, the star shape can be stabilized.

It has been known that insufficient edge diffusion may lead to morphological instability.[51−53] Especially in our system, the sulfur concentration increases over time, which means that S/Mo atomic ratio is gradually increasing. As this ratio increases, similar to that occurred in ZnO epitaxial growth, the mobility of metal adatoms will be decreased.[54] Meanwhile, insufficient surface diffusion will lead to irregular edge morphology on the macroscopic scale. For MoS_2 growth, the edge diffusion length of the Mo atom can be estimated by:[55]

$$\lambda_{Mo} = \sqrt{D_e \times \tau_e} \quad (2)$$

where τ_e is the mean lifetime of the Mo adatoms on the crystal edge before detaching the edge and $D_e = \nu a^2 \exp(-E_{sd}/k_B T)$ is the diffusion coefficient along the crystal edge. ν is the vibrational frequency, a is the lattice constant, E_{sd} is the activation energy for the edge diffusion, k_B is the Boltzmann constant, and T is the substrate temperature. In our experiments, the substrate temperature is kept constant (800 °C). Hence, the temperature is not a variable in the edge diffusion length of the Mo atom. On the other hand, we assume that the sulfur atoms stabilize the mobile Mo adatoms along the edge of the MoS_2 flake by forming Mo−S bonds, resulting in incorporating Mo adatoms into the MoS_2 flake. Therefore, the average lifetime τ_e of Mo adatoms is determined by the time interval for the diffusing Mo adatoms on the edge before combining with S atoms.[51−53] This implies the S/Mo ratio plays a crucial role in the edge diffusion length of the Mo atom. The higher the S/Mo ratio, the higher the probability of Mo atoms being stabilized by sulfur atoms.[52,56] Consequently, the formation time of Mo-S bonds decreases with increasing S/Mo ratio. This means that the high S/Mo ratio leads to a shorter lifetime τ_e of Mo adatoms, making the edge diffusion length of Mo atom decrease according to eq 2.

Consequently, the edge diffusion length λ_{Mo} decreases with the increase in the S/Mo ratio. In the early stage of growth, evaporation of sulfur is not sufficient, and hence the S/Mo ratio is small. The Mo atoms can diffuse along the edge freely. However, the S/Mo ratio increases continuously over time. At the later stage of growth, the S/Mo ratio becomes significantly high, and hence the diffusion length λ_{Mo} decreases dramatically. It is known that the Mo atoms diffuse on the edge of the flake before they bond to S atoms, suggesting that the MoS_2 flake grows in a diffusion-limited regime. On the other hand, as presented in detail later in this section, first-principles calculations indicate that the nucleation energy barrier of a MoS_2 cluster at the corner of triangular MoS_2 crystallite becomes higher than in the central part of the edge. In other words, the central part of the edge of the triangular MoS_2 flake is the most favorable nucleation site. Therefore, at the later stage of growth, MoS_2 molecules are easier to nucleate in the central regions of the edges of the MoS_2 flakes. As the newborn nuclei develop larger, MoS_2 flake gradually changes the morphology from triangular to the bulgy irregular shape (Figure 6h-k). Generally, the variation of the S/Mo ratio affects the edge diffusion length and nucleation behavior on the edge of a 2D crystallite, leading to various growth morphologies. So far, our current experimental data do not show the clue of the substrate influence on the morphological evolution.

Now we focus on the nucleation process on the edge of the flakes. It has been known that twinning occurs in the kinetic growth of crystallites.[13,57] It is also well established that grain boundaries in the MoS_2 monolayer comprise various crystallographic defects, such as 5|7, 4|6, 4|8, and 6|8 rings.[41,58] Among these defects, 4|6 rings (illustrated in Figure 7b) are commonly

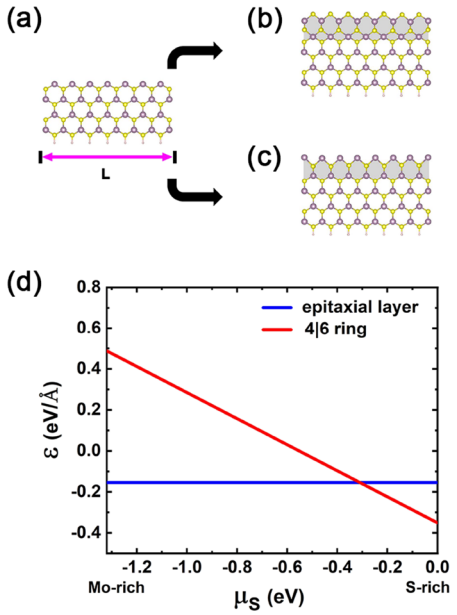

Figure 7. Schematic illustration of atomic structures of (a) the 7 × 3 MoS_2 supercell, (b) the 7 × 3 MoS_2 supercell after growing a layer with 4|6 ring (gray shaded area), and (c) the 7 × 3 MoS_2 supercell after growing an epitaxial layer of MoS_2 unit (gray shaded area). The purple and yellow circles denote the Mo and S atoms, respectively. The zigzag S-terminated edge of the MoS_2 supercell is fully hydronated. L represents the length of the MoS_2 supercell. (d) The formation energies of an epitaxial layer of MoS_2 unit and a layer with 4|6 ring as a function of the sulfur chemical potential μ_S.

formed in MoS_2 twin crystallites.[58,59] The 4|6 ring contains four Mo atoms and eight S atoms, with two Mo−S bonds shared by the four- and sixfold rings. To gain further insight into the formation of this 4|6 ring in MoS_2 twin crystallites, we study its formation energy by first-principles calculations. For comparison, we also investigate the formation energy of a MoS_2 cluster, which nucleates epitaxially at the edge of MoS_2 crystallite without forming any defects. In both scenarios, nucleation at the zigzag Mo-terminated edge of the MoS_2 ribbon is considered, as illustrated in Figure 7b,c. The zigzag S-terminated edge of the MoS_2 ribbon is fully hydronated to stabilize this edge. The MoS_2 ribbon (shown in Figure 7a) is simulated by a 7 × 3 supercell (7-unit-cell long and 3-unit-cell wide) with periodic boundary conditions. Here all the atomic positions in the studied configurations are fully relaxed. The formation energy renormalized by the length of the MoS_2 ribbon is defined as

$$\varepsilon = (E_\alpha - E_{pri} - n_{Mo}\mu_{Mo} - n_s\mu_s)/L \quad (3)$$

where E_α is the total energy of the 7 × 3 MoS_2 supercell after growing a layer with 4|6 ring or an epitaxial layer of MoS_2 unit on its edge, E_{pri} is the energy of the pristine 7 × 3 MoS_2 supercell, n_{Mo} and n_s are the number of added molybdenum and sulfur atoms on the edge of the MoS_2 supercell, respectively, μ_{Mo} and μ_s represent the chemical potential of molybdenum and sulfur, respectively, L is the length of the MoS_2 supercell (Figure 7a). In a thermal equilibrium scenario,

https://doi.org/10.1021/acs.jpcc.1c10342
J. Phys. Chem. C 2022, 126, 3549−3559

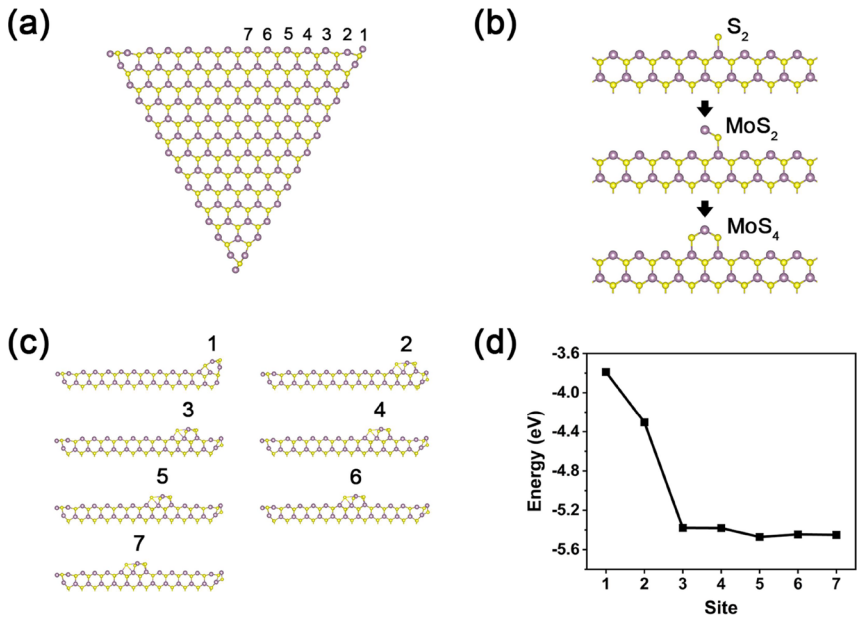

Figure 8. (a) Top view of the triangular MoS_2 crystallite with zigzag Mo-terminated edges. The purple and yellow circles denote the Mo and S atoms, respectively. (b) Schematic illustration of a hexagonal kink (MoS_4 cluster) nucleation processes at the zigzag Mo-terminated edge. (c) Schematic illustration of a MoS_4 cluster nucleating at the different sites of the zigzag Mo-terminated edge after relaxation. (d) The calculated formation energy of a MoS_4 cluster at the different sites of the zigzag Mo-terminated edge.

the chemical potential of molybdenum and sulfur satisfy the equation $\mu_{Mo} + 2\mu_s \approx E_{Mo} + 2E_S + \Delta H_f = E_{MoS_2}$, where E_{Mo} is the energy of a single Mo atom in the metallic body-centered cubic molybdenum structure, E_S is the energy of a single S atom in the bulk orthorhombic sulfur structure, and ΔH_f is the formation heat of a MoS_2 unit, and E_{MoS_2} is the total energy of a MoS_2 unit.[19,44] Then, eq 3 can be rewritten as

$$\varepsilon = [E_\alpha - E_{pri} - n_{Mo}E_{MoS_2} + (2n_{Mo} - n_s)\mu_s]/L \quad (4)$$

To avoid the formation of solid sulfur and metallic molybdenum, the allowed region for the values of μ_S is $E_S + \Delta H_f/2 \le \mu_S \le E_S$. The heat of formation ΔH_f is estimated to be −2.64 eV. We choose the maximum value of μ_S to be zero, corresponding to the sulfur-rich condition. Thus, the minimum value of μ_S is equal to −1.32 eV, corresponding to the molybdenum-rich condition.[19,44] According to eq 4, the formation energy of the 4|6 ring nucleated at the edge of MoS_2 crystallite can be expressed as $\varepsilon_1 = (E_\alpha - E_{pri} - 7E_{MoS_2} - 14\mu_s)/L$, and the formation energy of the MoS_2 unit epitaxially nucleated at the edge of MoS_2 crystallite can be expressed as $\varepsilon_2 = (E_\alpha - E_{pri} - 7E_{MoS_2})/L$. The formation energies as a function of μ_s are plotted in Figure 7d. One may find that the formation energy of the 4|6 ring is lower than that of an epitaxial MoS_2 cluster when μ_s is near the right end, i.e., in the sulfur-rich region (it is worth noting that calculating the formation energy of different MoS_2 clusters at a given S/Mo ratio is beyond the capacity of current first-principles calculations). Our calculations imply that 4|6 rings are likely formed on the zigzag Mo-terminated edge of MoS_2 crystallite in sulfur-rich conditions. In other words, twinning can be easily formed on the edge of MoS_2 flake in sulfur-rich conditions. In this case, the lattice orientation of the newborn layer has been rotated for 60° with respect to the original ribbon (Figure 7b). Consequently, once a newborn nucleus appears on the edge of the triangular MoS_2 flake, the nucleus also should evolve to a triangular shape in the sulfur-rich conditions (Figure 6d,e). The lattice orientation of newborn crystallite has been rotated for 60° with respect to the original MoS_2 flake (illustrated in Figure 3f). Thus, the twin boundaries are formed in this way, as described in Figure 6f. As the clusters with 4|6 rings develop larger, the shape of the nucleus gradually evolves into a rhomb (Figure 6g). By repeating this process on the edge of MoS_2 flakes, a transition to an irregular bulgy shape occurs (Figure 6h−k).

For a two-dimensional crystalline flake, the atomic environment at the corner and in the central part of the edge is different. Let us consider a triangular MoS_2 flake with Mo-terminated edges, which contains 13 MoS_2 molecules along each edge, as illustrated in Figure 8a. For an atom located at the corner, the number of surrounding atoms is fewer than in the central part of the edge. Consequently, we expect more dangling bonds at the corner of the triangular flake, resulting in higher local edge free energy. We calculate the formation energy of a MoS_2 cluster nucleating at the different sites along a zigzag Mo-terminated edge. Following the kink nucleation and kink propagation approach, we introduce S_2 (sulfur dimer) and Mo on the edge of the MoS_2 flake.[60,61] As illustrated in Figure 8b, S_2 is first attached to the zigzag Mo-terminated edge. Then, a Mo atom is attached to bond S atoms at the edge, forming the energetically favorable armchair site of S. In sulfur-rich conditions, the armchair sites are easily occupied by S_2 to form a hexagonal kink. Previous studies have demonstrated that once a hexagonal kink is nucleated at the edges, the kink propagation is fast due to the lower diffusion energy barrier.[60,61] Here, we calculate the total energy of the triangular MoS_2 crystallite when a hexagonal kink (MoS_4 cluster) nucleates at different sites of the zigzag Mo-terminated edge. In our first-principles calculations, the triangular MoS_2 crystallite and the MoS_4 cluster are fully relaxed (Figure 8c). The formation energy of the MoS_4 cluster on the edge of triangular MoS_2 flake is expressed as:

$$\Delta E(x) = E_{total}(x) - E_{triangle} - E_{Mo} - 4E_S \quad (5)$$

https://doi.org/10.1021/acs.jpcc.1c10342
J. Phys. Chem. C 2022, 126, 3549−3559

where E_{total} is the total energy of a triangular MoS_2 crystallite with a MoS_4 cluster, $E_{triangle}$ is the energy of a triangular MoS_2 flake, E_{Mo} and E_S are the energies of a single Mo and S atom in the most stable bulk structures, respectively, and x is the nucleation site on the zigzag Mo-terminated edge (Figure 8c). As illustrated in Figure 8d, the formation energy is the largest when a MoS_4 cluster nucleates at the vertex (site 1) of the MoS_2 crystallite. The formation energy of the MoS_4 cluster decreases significantly when the cluster nucleates in the central part of the edge. This means that the nucleation energy barrier at the corner region of a triangular MoS_2 crystallite is larger than that in the central part of the edge. This effect promotes nucleation in the central part of the edge and gradually drives the morphology of the MoS_2 flake from a triangle to a bulgy pattern.

It is known that the charge density state strongly affects PL intensity in TMDs.[18,62] Since MoS_2 crystal is usually n-type doped,[9,62] the photogenerated electron−hole pair (neutral exciton) can bind with an electron to form a negatively charged exciton (negative trion). In the presence of high excess electrons, the PL process in MoS_2 is dominated by trion recombination, and most photogenerated electrons and holes are forced to recombine nonradiatively.[63] Meanwhile, the PL intensity of monolayer MoS_2 is low. However, the crystalline defects of TMDs are very sensitive to gas molecules and can act as active adsorption sites due to the strong electronic interaction between defects and gas molecules.[63,64] Consequently, when PL measurements are performed in the ambient environment, O_2 and H_2O in the air can easily adsorb at the defect sites. Meanwhile, electrons can be transferred from MoS_2 to the adsorbed molecules, generating effective p-type doping at the absorption site.[63,65] Due to the depletion of excess electrons in MoS_2, neutral excitons are stabilized while negative trions are depleted, which switches the dominant PL process in MoS_2 from trion recombination to exciton recombination.[63,65] Furthermore, crystalline defects in 2D structures can trap charge carriers and localize excitons.[64] The localized exciton at defect sites of TMDs has large binding energy, which can prevent thermo-activated nonradiative recombination.[65] These effects would lead to an enhanced PL emission intensity. For the MoS_2 flakes with the star shape or triangular shape, their corner and edge regions have many dangling bonds, which act as the active adsorption centers.[13,66] Thus, the substantial enhancement of PL intensity occurs at corners and edges due to the preferential attachment of adsorbates in these regions (Figure 5a,b). It has been known that the PL intensity in MoS_2 flakes increases with the increase of local defect concentration.[64,66] Therefore, we expect the inhomogeneous enhancement of PL intensity at some corner and edge regions may be associated with the inhomogeneous distribution of defects in the as-grown MoS_2 flakes. For the irregular bulgy MoS_2 flakes, the structural analysis indicates that they contain many twin grain boundaries (Figure 3f,g). We believe that repeated twinning is the primary approach to transform the crystallite from triangular faceted crystallite to bulgy irregular-shaped flake (Figure 6h−k). Previous studies have shown that the twin boundaries possess abundant sulfur vacancies and can be considered as active adsorption sites as well for molecule adsorption.[13,66] With a large number of twinning boundaries in the bulgy irregular-shaped MoS_2 flakes, strong PL intensity may appear in the central part of the flake (Figure 5c). However, currently it remains unclear how to compare the PL emission intensity in the central part of the crystallite and that from the edge and corner regions of the flakes.

CONCLUSIONS

To summarize, we have synthesized monolayer MoS_2 flakes on the optical glass substrate. As time goes on, the growth morphology of MoS_2 flakes undergoes a transition from triangle to three-point star, then to triangle, and finally to the bulgy irregular shape when the temperature of sulfur powder is set as 140 °C. Structural analysis indicates that the MoS_2 flakes with three-point-star shape and triangular shape are all single-crystalline, the bulgy irregular-shaped MoS_2 flakes contain many grain boundaries and are essentially polycrystalline. By tuning the growth time and temperature of the sulfur powder, the atomic ratio of S and Mo can be adjusted on the growing interface. The variation of the S/Mo ratio affects the edge diffusion length and nucleation behavior on the edge of crystallite, leading to various growth morphologies. Optical measurements showed that the photoluminescence intensity of MoS_2 flakes strongly correlates with their morphology. We suggest these observations enrich the understanding of the morphology evolution of MoS_2 flakes and the formation of twinning in MoS_2 flakes. This work also provides a clue to controllably synthesize TMD flakes with a specific morphology.

ASSOCIATED CONTENT

Supporting Information

The Supporting Information is available free of charge at https://pubs.acs.org/doi/10.1021/acs.jpcc.1c10342.

Optical micrographs of the MoS_2 flakes at different locations across the substrate, photoluminescence spectra measured with different excitation power on the MoS_2 flakes with different shapes, and PL mapping of MoS_2 flake with different scanning directions (PDF)

AUTHOR INFORMATION

Corresponding Authors

Ruwen Peng − *National Laboratory of Solid State Microstructures, School of Physics, and Collaborative Innovation Center of Advanced Microstructures, Nanjing University, Nanjing 210093, China;* orcid.org/0000-0003-0424-2771; Email: rwpeng@nju.edu.cn

Mu Wang − *National Laboratory of Solid State Microstructures, School of Physics, and Collaborative Innovation Center of Advanced Microstructures, Nanjing University, Nanjing 210093, China; American Physical Society, Ridge, New York 11961, United States;* orcid.org/0000-0002-3823-1272; Email: muwang@nju.edu.cn

Authors

Qingxuan Li − *National Laboratory of Solid State Microstructures, School of Physics, and Collaborative Innovation Center of Advanced Microstructures, Nanjing University, Nanjing 210093, China*

Lei Zhang − *National Laboratory of Solid State Microstructures, School of Physics, and Collaborative Innovation Center of Advanced Microstructures, Nanjing University, Nanjing 210093, China*

Chengyao Li − *National Laboratory of Solid State Microstructures, School of Physics, and Collaborative*

https://doi.org/10.1021/acs.jpcc.1c10342
J. Phys. Chem. C 2022, 126, 3549−3559

Innovation Center of Advanced Microstructures, Nanjing University, Nanjing 210093, China

Jie He − *National Laboratory of Solid State Microstructures, School of Physics, and Collaborative Innovation Center of Advanced Microstructures, Nanjing University, Nanjing 210093, China*

Yifan Wei − *National Laboratory of Solid State Microstructures, Jiangsu Key Laboratory of Artificial Functional Materials, College of Engineering and Applied Sciences and Collaborative Innovation Center of Advanced Microstructures, Nanjing University, Nanjing 210093, China*

Jinzhu Zhao − *Guangdong Provincial Key Laboratory of Quantum Engineering and Quantum Materials, School of Physics and Telecommunication Engineering and Guangdong-Hong Kong Joint Laboratory of Quantum Matter, South China Normal University, Guangzhou 510006, China;* orcid.org/0000-0003-1841-1302

Ruili Zhang − *National Laboratory of Solid State Microstructures, School of Physics, and Collaborative Innovation Center of Advanced Microstructures, Nanjing University, Nanjing 210093, China*

Peng Wang − *National Laboratory of Solid State Microstructures, Jiangsu Key Laboratory of Artificial Functional Materials, College of Engineering and Applied Sciences and Collaborative Innovation Center of Advanced Microstructures, Nanjing University, Nanjing 210093, China*

Shaojie Fu − *National Laboratory of Solid State Microstructures, School of Physics, and Collaborative Innovation Center of Advanced Microstructures, Nanjing University, Nanjing 210093, China*

Fei Chen − *National Laboratory of Solid State Microstructures, School of Physics, and Collaborative Innovation Center of Advanced Microstructures, Nanjing University, Nanjing 210093, China*

Complete contact information is available at: https://pubs.acs.org/10.1021/acs.jpcc.1c10342

Notes

The authors declare no competing financial interest.

■ ACKNOWLEDGMENTS

The authors would like to acknowledge funding support from the National Key R&D Program of China (2020YFA0211300, 2017YFA0303702), and the National Natural Science Foundation of China (11634005, 11974177, 61975078, 11874199).

■ REFERENCES

(1) Lopez-Sanchez, O.; Lembke, D.; Kayci, M.; Radenovic, A.; Kis, A. Ultrasensitive Photodetectors Based on Monolayer MoS_2. *Nat. Nanotechnol.* **2013**, *8*, 497−501.

(2) Xiao, D.; Liu, G. -B.; Feng, W. X.; Xu, X. D.; Yao, W. Coupled Spin and Valley Physics in Monolayers of MoS_2 and Other Group-VI Dichalcogenides. *Phys. Rev. Lett.* **2012**, *108*, No. 196802.

(3) Xu, X. D.; Yao, W.; Xiao, D.; Heinz, T. F. Spin and Pseudospins in Layered Transition Metal Dichalcogenides. *Nat. Phys.* **2014**, *10*, 343−350.

(4) Jaramillo, T. F.; Jørgensen, K. P.; Bonde, J.; Nielsen, J. H.; Horch, S.; Chorkendorff, I. Identification of Active Edge Sites for Electrochemical H_2 Evolution from MoS_2 Nanocatalysts. *Science* **2007**, *317*, 100−102.

(5) Shi, J. P.; Ma, D. L.; Han, G. -F.; Zhang, Y.; Ji, Q. Q.; Gao, T.; Sun, J. Y.; Song, X. J.; Li, C.; Zhang, Y. S. Controllable Growth and Transfer of Monolayer MoS_2 on Au Foils and Its Potential Application in Hydrogen Evolution Reaction. *ACS Nano* **2014**, *8*, 10196−10204.

(6) Chen, J. Y.; Zhao, X. X.; Tan, S. J. R.; Xu, H.; Wu, B.; Liu, B.; Fu, D. Y.; Fu, W.; Geng, D. C.; Liu, Y. P. Chemical Vapor Deposition of Large-Size Monolayer $MoSe_2$ Crystals on Molten Glass. *J. Am. Chem. Soc.* **2017**, *139*, 1073−1076.

(7) Gao, Q. G.; Zhang, Z. F.; Xu, X. L.; Song, J.; Li, X. F.; Wu, Y. Q. Scalable High Performance Radio Frequency Electronics Based on Large Domain Bilayer MoS_2. *Nat. Commun.* **2018**, *9*, 4778.

(8) Cai, Z. Y.; Liu, B. L.; Zou, X. L.; Cheng, H. -M. Chemical Vapor Deposition Growth and Applications of Two-Dimensional Materials and Their Heterostructures. *Chem. Rev.* **2018**, *118*, 6091−6133.

(9) Yang, P. F.; Zou, X. L.; Zhang, Z. P.; Hong, M.; Shi, J. P.; Chen, S. L.; Shu, J. P.; Zhao, L. Y.; Jiang, S. L.; Zhou, X. B. Batch Production of 6-Inch Uniform Monolayer Molybdenum Disulfide Catalyzed by Sodium in Glass. *Nat. Commun.* **2018**, *9*, 979.

(10) Wang, S. S.; Rong, Y. M.; Fan, Y.; Pacios, M.; Bhaskaran, H.; He, K.; Warner, J. H. Shape Evolution of Monolayer MoS_2 Crystals Grown by Chemical Vapor Deposition. *Chem. Mater.* **2014**, *26*, 6371−6379.

(11) Yang, S. Y.; Shim, G. W.; Seo, S. -B.; Choi, S. -Y. Effective Shape-Controlled Growth of Monolayer MoS_2 Flakes by Powder-Based Chemical Vapor Deposition. *Nano Res.* **2017**, *10*, 255−262.

(12) Zhang, Y.; Ji, Q. Q.; Han, G. -F.; Ju, J.; Shi, J. P.; Ma, D. L.; Sun, J. Y.; Zhang, Y. S.; Li, M. J.; Lang, X. -Y. Dendritic, Transferable, Strictly Monolayer MoS_2 Flakes Synthesized on $SrTiO_3$ Single Crystals for Efficient Electrocatalytic Applications. *ACS Nano* **2014**, *8*, 8617−8624.

(13) Wang, J. W.; Cai, X. B.; Shi, R.; Wu, Z. F.; Wang, W. J.; Long, G.; Tang, Y. J.; Cai, N. D.; Ouyang, W. K.; Geng, P. Twin Defect Derived Growth of Atomically Thin MoS_2 Dendrites. *ACS Nano* **2018**, *12*, 635−643.

(14) Cai, Z. Y.; Shen, T. Z.; Zhu, Q.; Feng, S. M.; Yu, Q. M.; Liu, J. M.; Tang, L.; Zhao, Y.; Wang, J. W.; Liu, B. L. Dual-Additive Assisted Chemical Vapor Deposition for the Growth of Mn-Doped 2D MoS_2 with Tunable Electronic Properties. *Small* **2020**, *16*, No. 1903181.

(15) Li, S. S.; Lin, Y. -C.; Zhao, W.; Wu, J.; Wang, Z.; Hu, Z. H.; Shen, Y. D.; Tang, D. -M.; Wang, J. Y.; Zhang, Q. Vapour-Liquid-Solid Growth of Monolayer MoS_2 Nanoribbons. *Nat. Mater.* **2018**, *17*, 535−542.

(16) Xu, W. S.; Li, S.; Zhou, S.; Lee, J. K.; Wang, S. S.; Sarwat, S. G.; Wang, X. C.; Bhaskaran, H.; Pasta, M.; Warner, J. H. Large Dendritic Monolayer MoS_2 Grown by Atmospheric Pressure Chemical Vapor Deposition for Electrocatalysis. *ACS Appl. Mater. Interfaces* **2018**, *10*, 4630−4639.

(17) Ma, J.; Li, X. Y.; Gan, L.; Zhang, S. P.; Cao, Y. F.; Nie, Z. W.; Wang, X. N.; Ma, D. L.; He, L.; Nie, J. C. Controlling the Dendritic Structure and the Photo-Electrocatalytic Properties of Highly Crystalline MoS_2 on Sapphire Substrate. *2D Mater.* **2018**, *5*, No. 031015.

(18) van der Zande, A. M.; Huang, P. Y.; Chenet, D. A.; Berkelbach, T. C.; You, Y.; Lee, G. -H.; Heinz, T. F.; Reichman, D. R.; Muller, D. A.; Hone, J. C. Grains and Grain Boundaries in Highly Crystalline Monolayer Molybdenum Disulphide. *Nat. Mater.* **2013**, *12*, 554−561.

(19) Cao, D.; Shen, T.; Liang, P.; Chen, X. S.; Shu, H. B. Role of Chemical Potential in Flake Shape and Edge Properties of Monolayer MoS_2. *J. Phys. Chem. C* **2015**, *119*, 4294−4301.

(20) Ji, Q. Q.; Zhang, Y.; Shi, J. P.; Sun, J. Y.; Zhang, Y. F.; Liu, Z. F. Morphological Engineering of CVD-Grown Transition Metal Dichalcogenides for Efficient Electrochemical Hydrogen Evolution. *Adv. Mater.* **2016**, *28*, 6207−6212.

(21) Zhao, X. X.; Fu, D. Y.; Ding, Z. J.; Zhang, Y. -Y.; Wan, D. Y.; Tan, S. J. R.; Chen, Z. X.; Leng, K.; Dan, J. D.; Fu, W. Mo-Terminated Edge Reconstructions in Nanoporous Molybdenum Disulfide Film. *Nano Lett.* **2018**, *18*, 482−490.

(22) Tan, S. J. R.; Abdelwahab, I.; Ding, Z.; Zhao, X.; Yang, T.; Loke, G. Z. J.; Lin, H.; Verzhbitskiy, I.; Poh, S. M.; Xu, H. Chemical Stabilization of 1T′ Phase Transition Metal Dichalcogenides with

Giant Optical Kerr Nonlinearity. *J. Am. Chem. Soc.* **2017**, *139*, 2504−2511.
(23) Zhang, S. P.; Li, X. Y.; Zhang, X. L.; Wang, X. N.; Wang, W. P.; Yu, R. C.; Cao, Y. M.; Zhang, D.; Wang, S. Y.; He, L. Enhancement of the Photoelectrocatalytic H_2 Evolution on a Rutile-TiO_2(001) Surface Decorated with Dendritic MoS_2 Monolayer Nanoflakes. *ACS Appl. Energy Mater.* **2020**, *3*, 5756−5764.
(24) Yin, X. B.; Ye, Z. L.; Chenet, D. A.; Ye, Y.; O'Brien, K.; Hone, J. C.; Zhang, X. Edge Nonlinear Optics on a MoS_2 Atomic Monolayer. *Science* **2014**, *344*, 488−490.
(25) Huang, Y. L.; Chen, Y. F.; Zhang, W. J.; Quek, S. Y.; Chen, C. -H.; Li, L. -J.; Hsu, W. -T.; Chang, W. -H.; Zheng, Y. J.; Chen, W. Bandgap Tunability at Single-Layer Molybdenum Disulphide Grain Boundaries. *Nat. Commun.* **2015**, *6*, 6298.
(26) Xu, H.; Liu, S. L.; Ding, Z. J.; Tan, S. J. R.; Yam, K. M.; Bao, Y.; Nai, C. T.; Ng, M. -F.; Lu, J.; Zhang, C. Oscillating Edge States in One-Dimensional MoS_2 Nanowires. *Nat. Commun.* **2016**, *7*, 12904.
(27) Li, Y. F.; Zhou, Z.; Zhang, S. B.; Chen, Z. F. MoS_2 Nanoribbons: High Stability and Unusual Electronic and Magnetic Properties. *J. Am. Chem. Soc.* **2008**, *130*, 16739−16744.
(28) Chen, K. Y.; Deng, J. K.; Ding, X. D.; Sun, J.; Yang, S.; Liu, J. Z. Ferromagnetism of 1T′-MoS_2 Nanoribbons Stabilized by Edge Reconstruction and Its Periodic Variation on Nanoribbons Width. *J. Am. Chem. Soc.* **2018**, *140*, 16206−16212.
(29) Lauritsen, J. V.; Bollinger, M. V.; Lægsgaard, E.; Jacobsen, K. W.; Nørskov, J. K.; Clausen, B. S.; Topsøe, H.; Besenbacher, F. Atomic-Scale Insight into Structure and Morphology Changes of MoS_2 Nanoclusters in Hydrotreating Catalysts. *J. Catal.* **2004**, *221*, 510−522.
(30) Zhang, Y.; Ji, Q. Q.; Wen, J. X.; Li, J.; Li, C.; Shi, J. P.; Zhou, X. B.; Shi, K. B.; Chen, H. J.; Li, Y. C. Monolayer MoS_2 Dendrites on a Symmetry-Disparate $SrTiO_3$ (001) Substrate: Formation Mechanism and Interface Interaction. *Adv. Funct. Mater.* **2016**, *26*, 3299−3305.
(31) Ju, M.; Liang, X. Y.; Liu, J. X.; Zhou, L.; Liu, Z.; Mendes, R. G.; Rümmeli, M. H.; Fu, L. Universal Substrate-Trapping Strategy to Grow Strictly Monolayer Transition Metal Dichalcogenides Crystals. *Chem. Mater.* **2017**, *29*, 6095−6103.
(32) Zhou, J. D.; Lin, J. H.; Huang, X. W.; Zhou, Y.; Chen, Y.; Xia, J.; Wang, H.; Xie, Y.; Yu, H. M.; Lei, J. C. A Library of Atomically Thin Metal Chalcogenides. *Nature* **2018**, *556*, 355−359.
(33) Chen, J. Y.; Zhao, X. X.; Grinblat, G.; Chen, Z. X.; Tan, S. J. R.; Fu, W.; Ding, Z. J.; Abdelwahab, I.; Li, Y.; Geng, D. C. Homoepitaxial Growth of Large-Scale Highly Organized Transition Metal Dichalcogenide Patterns. *Adv. Mater.* **2018**, *30*, No. 1704674.
(34) Li, J. Z.; Chen, M. G.; Zhang, C. H.; Dong, H. C.; Lin, W. Y.; Zhuang, P. P.; Wen, Y.; Tian, B.; Cai, W. W.; Zhang, X. X. Fractal-Theory-Based Control of the Shape and Quality of CVD-Grown 2D Materials. *Adv. Mater.* **2019**, *31*, No. 1902431.
(35) Li, X. Y.; Zhang, S. P.; Chen, S.; Zhang, X. L.; Gao, J. F.; Zhang, Y. -W.; Zhao, J. J.; Shen, X.; Yu, R. C.; Yang, Y. Mo Concentration Controls the Morphological Transitions from Dendritic to Semi-compact, and to Compact Growth of Monolayer Crystalline MoS_2 on Various Substrates. *ACS Appl. Mater. Interfaces* **2019**, *11*, 42751−42759.
(36) Huang, L. L.; Thi, Q. H.; Zheng, F. Y.; Chen, X.; Chu, Y. W.; Lee, C. -S.; Zhao, J.; Ly, T. H. Catalyzed Kinetic Growth in Two-Dimensional MoS_2. *J. Am. Chem. Soc.* **2020**, *142*, 13130−13135.
(37) Li, H.; Zhang, Q.; Yap, C. C. R.; Tay, B. K.; Edwin, T. H. T.; Olivier, A.; Baillargeat, D. From Bulk to Monolayer MoS_2: Evolution of Raman Scattering. *Adv. Funct. Mater.* **2012**, *22*, 1385−1390.
(38) Lee, Y. -H.; Zhang, X. -Q.; Zhang, W.; Chang, M. -T.; Lin, C. -T.; Chang, K. -D.; Yu, Y. -C.; Wang, J. -T. W.; Chang, C. -S.; Li, L. -J. Synthesis of Large-Area MoS_2 Atomic Layers with Chemical Vapor Deposition. *Adv. Mater.* **2012**, *24*, 2320−2325.
(39) Shi, Y. M.; Zhou, W.; Lu, A. -Y.; Fang, W. J.; Lee, Y. -H.; Hsu, A. L.; Kim, S. M.; Kim, K. K.; Yang, H. Y.; Li, L. -J. van der Waals Epitaxy of MoS_2 Layers Using Graphene As Growth Templates. *Nano Lett.* **2012**, *12*, 2784−2791.
(40) Wan, W.; Zhan, L. J.; Xu, B. B.; Zhao, F.; Zhu, Z. W.; Zhou, Y. H.; Yang, Z. L.; Shin, T.; Cai, W. W. Temperature-Related Morphological Evolution of MoS_2 Domains on Graphene and Electron Transfer within Heterostructures. *Small* **2017**, *13*, No. 1603549.
(41) Najmaei, S.; Liu, Z.; Zhou, W.; Zou, X. L.; Shi, G.; Lei, S. D.; Yakobson, B. I.; Idrobo, J. -C.; Ajayan, P. M.; Lou, J. Vapour Phase Growth and Grain Boundary Structure of Molybdenum Disulphide Atomic Layers. *Nat. Mater.* **2013**, *12*, 754−759.
(42) Liu, H. C.; Zhu, Y. H.; Meng, Q. L.; Lu, X. W.; Kong, S.; Huang, Z. W.; Jiang, P.; Bao, X. H. Role of the Carrier Gas Flow Rate in Monolayer MoS_2 Growth by Modified Chemical Vapor Deposition. *Nano Res.* **2017**, *10*, 643−651.
(43) Byskov, L. S.; Nørskov, J. K.; Clausen, B. S.; Topsøe, H. Edge Termination of MoS_2 and CoMoS Catalyst Particles. *Catal. Lett.* **2000**, *64*, 95−99.
(44) Schweiger, H.; Raybaud, P.; Kresse, G.; Toulhoat, H. Shape and Edge Sites Modifications of MoS_2 Catalytic Nanoparticles Induced by Working Conditions: A Theoretical Study. *J. Catal.* **2002**, *207*, 76−87.
(45) Xiao, R. F.; Alexander, J. I. D.; Rosenberger, F. Growth Morphology with Anisotropic Surface Kinetics. *J. Cryst. Growth* **1990**, *100*, 313−329.
(46) Yokoyama, E.; Kuroda, T. Pattern Formation in Growth of Snow Crystals Occurring in the Surface Kinetic Process and the Diffusion Process. *Phys. Rev. A* **1990**, *41*, 2038−2049.
(47) Wang, Y.; Khachaturyan, A. G. Shape Instability During Precipitate Growth in Coherent Solids. *Acta Metal. Mater.* **1995**, *43*, 1837−1857.
(48) Chernov, A. A. Stability of Faceted Shapes. *J. Cryst. Growth* **1974**, *24-25*, 11−31.
(49) Wang, M.; Peng, R. -W.; Bennema, P.; Ming, N. -B. Morphological Instability of Crystals Grown from Thin Aqueous Solution Films with a Free Surface. *Philos. Mag. A* **1995**, *71*, 409−419.
(50) Wang, M.; Wildburg, G.; van Esch, J. H.; Bennema, P.; Nolte, R. J. M.; Rinsdorf, H. Surface-Tension-Gradient-Induced Pattern Formation in Monolayers. *Phys. Rev. Lett.* **1993**, *71*, 4003−4006.
(51) Geng, D. C.; Meng, L.; Chen, B. Y.; Gao, E. L.; Yan, W.; Yan, H.; Luo, B.; Xu, J.; Wang, H. P.; Mao, Z. P. Controlled Growth of Single-Crystal Twelve-Pointed Graphene Grains on a Liquid Cu Surface. *Adv. Mater.* **2014**, *26*, 6423−6429.
(52) Nie, Y. F.; Liang, C. P.; Zhang, K. H.; Zhao, R.; Eichfeld, S. M.; Cha, P. -R.; Colombo, L.; Robinson, J. A.; Wallace, R. M.; Cho, K. First Principles Kinetic Monte Carlo Study on the Growth Patterns of WSe_2 Monolayer. *2D Mater.* **2016**, *3*, No. 025029.
(53) Pimpinelli, A.; Ferrando, R. Reentrant Morphological Instability of Epitaxial Islands. *Phys. Rev. B* **1999**, *60*, 17016−17022.
(54) Chen, Y.; Ko, H.-J.; Hong, S.-K.; Yao, T.; Segawa, Y. Morphology Evolution of ZnO($000\bar{1}$) Surface During Plasma-Assisted Molecular-Beam Epitaxy. *Appl. Phys. Lett.* **2002**, *80*, 1358−1360.
(55) Markov, I. V. *Crystal Growth for Beginners: Fundamentals of Nucleation, Cystal Growth and Epitaxy;* 2nd ed.; World Scientific Publishing: Singapore, 2006.
(56) Heyn, C.; Franke, T.; Anton, R.; Harsdorff, M. Correlation Between Island-Formation Kinetics, Surface Roughening, and RHEED Oscillation Damping During GaAs Homoepitaxy. *Phys. Rev. B* **1997**, *56*, 13483−13489.
(57) Xia, Y. N.; Xiong, Y. J.; Lim, B.; Skrabalak, S. E. Shape-Controlled Synthesis of Metal Nanocrystals: Simple Chemistry Meets Complex Physics? *Angew. Chem., Int. Ed.* **2009**, *48*, 60−103.
(58) Zhou, W.; Zou, X. L.; Najmaei, S.; Liu, Z.; Shi, Y. M.; Kong, J.; Lou, J.; Ajayan, P. M.; Yakobson, B. I.; Idrobo, J. -C. Intrinsic Structural Defects in Monolayer Molybdenum Disulfide. *Nano Lett.* **2013**, *13*, 2615−2622.
(59) Zou, X. L.; Liu, Y. Y.; Yakobson, B. I. Predicting Dislocations and Grain Boundaries in Two-Dimensional Metal-Disulfides from the First Principles. *Nano Lett.* **2013**, *13*, 253−258.

https://doi.org/10.1021/acs.jpcc.1c10342
J. Phys. Chem. C 2022, 126, 3549−3559

(60) Artyukhov, V. I.; Liu, Y.; Yakobson, B. I. Equilibrium at the Edge and Atomistic Mechanisms of Graphene Growth. *Proc. Natl. Acad. Sci. U. S. A.* **2012**, *109*, 15136−15140.
(61) Chen, S.; Gao, J. F.; Srinivasan, B. M.; Zhang, G.; Sorkin, V.; Hariharaputran, R.; Zhang, Y. -W. Origin of Ultrafast Growth of Monolayer WSe_2 via Chemical Vapor Deposition. *npj Comput. Mater.* **2019**, *5*, 28.
(62) Mak, K. F.; He, K.; Lee, C.; Lee, G. H.; Hone, J.; Heinz, T. F.; Shan, J. Tightly Bound Trions in Monolayer MoS_2. *Nat. Mater.* **2013**, *12*, 207−211.
(63) Tongay, S.; Zhou, J.; Ataca, C.; Liu, J.; Kang, J. S.; Matthews, T. S.; You, L.; Li, J.; Grossman, J. C.; Wu, J. Broad-Range Modulation of Light Emission in Two-Dimensional Semiconductors by Molecular Physisorption Gating. *Nano Lett.* **2013**, *13*, 2831−2836.
(64) Tongay, S.; Suh, J.; Ataca, C.; Fan, W.; Luce, A.; Kang, J. S.; Liu, J.; Ko, C.; Raghunathanan, R.; Zhou, J. Defects Activated Photoluminescence in Two-Dimensional Semiconductors: Interplay between Bound, Charged, and Free Excitons. *Sci. Rep.* **2013**, *3*, 2657.
(65) Nan, H. Y.; Wang, Z. L.; Wang, W. H.; Liang, Z.; Lu, Y.; Chen, Q.; He, D. W.; Tan, P. H.; Miao, F.; Wang, X. R. Strong Photoluminescence Enhancement of MoS_2 through Defect Engineering and Oxygen Bonding. *ACS Nano* **2014**, *8*, 5738−5745.
(66) Zhang, G. Z.; Wang, J. W.; Wu, Z. F.; Shi, R.; Ouyang, W. K.; Amini, A.; Chandrashekar, B. N.; Wang, N.; Cheng, C. Shape-Dependent Defect Structures of Monolayer MoS_2 Crystals Grown by Chemical Vapor Deposition. *ACS Appl. Mater. Interfaces* **2017**, *9*, 763−770.

https://doi.org/10.1021/acs.jpcc.1c10342
J. Phys. Chem. C 2022, 126, 3549−3559